Multifunctional ultrasmall nanoplatforms for vascular-targeted interstitial photodynamic therapy of brain tumors guided by real-time MRI

Denise Bechet, Florent Auger, Pierre Couleaud, Eric Marty, Laura Ravasi, Nicolas Durieux, Corinne Bonnet, François Plénat, Céline Frochot, Serge R. Mordon, et al.

MULTIFUNCTIONAL ULTRASMALL NANOPLATFORMS FOR VASCULAR-TARGETED INTERSTITIAL PHOTODYNAMIC THERAPY OF BRAIN TUMORS GUIDED BY REAL-TIME MRI

Denise Bechet[1,2], Florent Auger[3], Pierre Couleaud[4,5], Eric Marty[6], Laura Ravasi[3], Nicolas Durieux[3], Corinne Bonnet[7], François Plénat[1,2,7], Céline Frochot[4,5,*], Serge Mordon[8,*], Olivier Tillement[7], Régis Vanderesse[10,11], François Lux[9], Pascal Perriat[9], François Guillemin[1,2,*], Muriel Barberi-Heyob[1,2*]

[1] CRAN UMR 7039, CNRS, Vandœuvre-lès-Nancy, France
[2] CRAN UMR 7039, Université de Lorraine, Vandœuvre-lès-Nancy, France
[3] IMPRT (Institut de Médecine Prédictive et de Recherche Thérapeutique) IFR 114, U 837 INSERM, CHRU de Lille, Lille, France
[4] LRGP UMR 7274, CNRS, Nancy, France
[5] LRGP UMR 7274, Université de Lorraine, Nancy, France
[6] Private executive, Marcilly-sur-Eure, France
[7] Laboratoire d'Anatomopathologie, CHU, Vandœuvre-lès-Nancy
[8] INSERM U703, Lille University Hospital, Lille
[9] LPCML UMR 5620 CNRS, Claude Bernard-University, Lyon, France
[10] LCPM FRE 3564, CNRS, Nancy, France
[11] LCPM FRE 3564, Université de Lorraine, Nancy, France
* GDR 3049 "Médicaments Photoactivables - Photochimiothérapie (PHOTOMED)"

Number of text pages, including references: 24
Number of figures: 7
Number of supplementary figures: 2
Number of references: 64
Number of words in abstract: 147
Number of words in Background: 995
Number of words in Methods: 1186
Number of words in Results: 1652
Number of words in Discussion: 1487
Total number of words including Figure legends: 6706

* *Corresponding author:* +33 (0)3 83 68 32 08 : muriel.barberi@univ-lorraine.fr; CRAN UMR 7039 CNRS, Département SBS, Faculté de Médecine - Bâtiment D, 1er étage, 9 avenue de la Forêt de Haye, BP 184, 54505 Vandœuvre-lès-Nancy

Acknowledgements: The authors would like to thank Jordane Jasniewski for size and zeta-potentiel measurements and Marc Verhille for his chemical assistance. This work was supported by the research funds of the French Ligue Nationale Contre le Cancer, ANR project no. ANR-08-PCVI-0021-01 Nano-VTP.

ABSTRACT

Photodynamic therapy (PDT) for brain tumors appears to be complementary to conventional treatments. Number studies show the major role of the vascular effect in the tumor eradication by PDT. For interstitial PDT (iPDT) of brain tumors guided by real-time imaging, multifunctional nanoparticles consisting of a surface-localized tumor vasculature targeting neuropilin-1 (NRP-1) peptide and encapsulated photosensitizer and magnetic resonance imaging (MRI) contrast agents, have been designed. Nanoplatforms confer photosensitivity to cells and demonstrate a molecular affinity to NRP-1. Intravenous injection into rats bearing intracranial glioma exhibited a dynamic contrast-enhanced MRI for angiogenic endothelial cells lining the neovessels mainly located in the peripheral tumor. By using MRI completed by NRP-1 protein expression of the tumor and brain adjacent to tumor tissues, we checked the selectivity of the nanoparticles. This study represents the first *in vivo* proof of concept of closed-head iPDT guided by real-time MRI using targeted ultrasmall nanoplatforms.

Keywords: multifunctional nanoplateforms, targeting, brain tumor, iPDT, real-time MRI

Abbreviations:

a.i.: arbitrary intensity ; a.u.: arbitrary unit ; ASL: Arterial Spin Labeling; ATWLPPR: H-Ala-Thr-Trp-Leu-Pro-Pro-Arg-OH; BAT: Brain Adjacent Tumor ; Cr: creatine ; CT: Computed Tomography ; DTPA: Diethylene Triamine Pentaacetic Acid ; DTPADA: Diethylenetriaminepentaacetic dianhydride ; EPI: Echo Planar Imaging ; FAIR: Flow-sensitive Alternating Inversion Recovery ; FDG: Fluoro-2-deoxyglucose ; FGR: Fluorescence-Guided Resection ; FLASH: Fast Low-Angle Shot ; FOV: Field of View ; HBSS: Hank's Buffered Salt Solution ; HER2: human epidermal growth factor receptor 2 ; HMGN2: high-mobility-group nucleosomal binding protein 2 ; ICP-MS: Inductively Coupled Plasma Mass Spectroscopy ; iPDT: interstitial PhotoDynamic Therapy ; LWRPTPA: H-Leu-Trp-Arg-Pro-Thr-Pro-Ala-OH ; MRI: Magnetic Resonance Imaging ; MRS: Magnetic Resonance Spectroscopy ; MTT: 3-(4,5-dimethylthiazol-2-yl)-2,5-diphenyl tetrazolium bromide ; NP: Nanoparticle ; NRP-1: Neuropilin-1 receptor ; PDD: Photodynamic Diagnosis ; PAS: Periodic-Acid-Schiff ; PET: Positron Emission Tomography ; PRESS: Point-Resolved Spectroscopy Sequence ; RGD: H-Arg-Gly-Asp-OH ; ROI: Region Of Interest ; ROS: Reactive Oxygen Species ; TE: Echo Time ; TPC: 5-(4-carboxyphenyl)-10,15,20-triphenylchlorin ; TPC-NHS: 5,10,15,tri-(p-tolyl)-20-(p-carboxylphenyl)chlorinsuccinidyl ester ; VEGF: Vascular Endothelial Growth Factor ; VTP: Vascular Targeted Photodynamic therapy ; Φ_f: fluorescence quantum yield ; Φ_Δ: $^1O_2$ quantum yield.

BACKGROUND

The poor outcome of primary malignant brain tumors is due to local invasion and local recurrence. Standard treatment of high-grade astrocytic tumors usually consists of cytoredictive surgery followed by radiation techniques and chemotherapy; however these tumor types usually recur despite treatments. Once progression of a tumor occurs, treatments options include repeat surgical resection, radiosurgery, chemotherapy with standard agents, novel therapies, or a combination of the above. Surgical resection is the mainstay of treatment removing tumor material with the aim of reducing intracranial pressure without worsening neurological function. However, in most cases curative resection is not possible due to infiltrating growth of the tumor into normal brain parenchyma.

The wide majority of glioblastoma multifome (GBM) recur locally and patients often succumb to and die from local recurrence, indicating that a more aggressive local therapy is required to eradicate it. However, complete radical surgical excision is hindered by the elusive nature of these tumors: a significant number of cells are not visible and require the aid of the surgical microscope. Moreover, side effects of radiotherapy can have considerable influence on health and quality of life. In this unfavorable context, photodynamic therapy (PDT) appears as an innovative technology being investigated to fulfill the need for a targeted cancer treatment that may reduce recurrence and extend survival with few side effects. PDT aims at selectively killing neoplastic lesions by the combined action of a photosensitizer and visible light whose combined action mainly results in the formation of ROS and singlet oxygen ($^1O_2$), which is thought to be the main mediator of cellular death induced by PDT.

A number of clinical studies, including phase-III randomized prospective clinical trials of PDT, have been reported, using different technologies such as photodynamic diagnosis (PDD), fluorescence-guided resection (FGR), interstitial PDT (iPDT) and intraoperative PDT.[1,2,3,4,5,6,7,8,9,10,11,12] Interstitial PDT offers a localized treatment approach in which improvements in local control of GBM may result in significant improved survival.[3,5,11] FGR promotes resection of the tumor and infiltrating areas which are not visible during conventional surgery, by taking into account the safety margins determined by the delineation of gross tumor volume and by planning the anatomical volume including the adjacent brain to tumor (BAT).

Destruction of the vasculature may indirectly lead to tumor eradication, following deprivation of life-sustaining nutrients and oxygen[13,14], and this effect is thought to play a major part in the destruction of some tumors by PDT.[15,16,17,18,19,20,21] Hence, tumor vasculature is a potential target of PDT damage. Receptors specifically located on angiogenic endothelial

cells, such as receptors to vascular endothelial growth factor (VEGF), can be used as molecular targets. We have previously described the conjugation of a chlorin (TPC) to an heptapeptide (ATWLPPR), specific for the VEGF receptor, neuropilin-1 (NRP-1).[22,23] We evidenced a significant decrease in the conjugated photosensitizer cellular uptake after RNA interference-mediated silencing of NRP-1.[24,25] This new targeted photosensitizer proved to be very efficient *in vitro* in human umbilical vein endothelial cells compared to its non-conjugated form.[23] *In vivo*, we demonstrated the interest of using this active-targeting strategy, allowing efficient tumor tissue uptake of the conjugated photosensitizer. In mice ectopically xenografted with U87 human malignant glioma cells, we evidenced that only the conjugated photosensitizer allowed a selective accumulation in endothelial cells of tumor vessels[26]. Thanks to an experimental design, an optimal vascular targeted PDT (VTP) condition was selected to show the effects and inter-dependence of photosensitizer dose, fluence and fluence rate on the growth of U87 cells ectopically xenografted in nude mice.[27] Using the peptide-conjugated photosensitizer, induction of tissue factor expression immediately post-treatment, led to the establishment of thrombogenic effects within the vessel *lumen.*[28]

As we previously described, non-biodegradable nanoparticles seem to be very promising careers satisfying all the requirements for an ideal targeted PDT.[29,30] We recently described the design and photophysical characteristics of multifunctional nanoparticles consisting of a surface-localized tumor vasculature targeting peptide and encapsulated PDT and imaging agents. The elaboration of these multifunctional silica-based nanoparticles was previously reported.[31] Nanoparticles functionalized with four peptides specifically bound to NRP-1 recombinant protein. Nanoparticles conferred photosensitivity to cells over-expressing NRP-1 receptor and provided evidence that the photosensitizer grafted within the nanoparticle matrix can be photo activated to induce cytotoxic effects *in vitro.*[31]

For the first time in this study, we challenged to validate the interest of multifunctional ultrasmall nanoplatforms, consisting of a surface-localized tumor vasculature targeting NRP-1 peptide and encapsulated PDT and imaging agents, for iPDT of brain tumors guided by interventional MRI. We developed and optimized ATWLPPR-targeted silica-based nanoparticles encapsulated gadolinium oxide as MRI contrast agent and a chlorin as a photosensitizer. More precisely, these hybrid non-biodegradable nanoparticles consisted of a gadolinium oxide core, a silica shell containing the covalently grafted chlorin molecules, diethylene triamine penta-acetic acids (DTPA, an active chelator substance) as surfactant and ATWLPPR (or LWRPTPA, a scramble peptide, as targeting units. Multifunctional

nanoparticles were evaluated in a series of *in vitro* experiments for their ability to produce $^1O_2$, to target NRP-1 recombinant protein, and to confer photosensitivity. Photodynamic activity of these nanoparticles resulted in the loss of cell viability related to chlorin concentration and light dose. *In vivo* studies revealed that nanoparticles could be visualized into rats bearing an orthotopic U87 using MRI analysis, leading to the optimization of the optical fiber implantation just before iPDT. Several clinical studies demonstrated that PET (Positron Emission Tomography) and CT (Computed Tomography), when used together, increased the diagnostic accuracy.[32,33,34] MRI, MRS (Magnetic Resonance Spectroscopy) and PET-CT allowed us to monitor post-iPDT effects, validating this concept of iPDT guided by MRI. We checked the functionalized nanoplatforms selectivity by determining NRP-1 protein expression into the tumor tissue related to MRI perfusion profile. After intravenous injection of ATWLPPR-targeted nanoplatforms, the positive contrast enhancement of the tumor by MRI allowed us to visualize the proliferating part of the tumor tissue compared to un-conjugated or LWRPTPA-conjugated nanoparticles.

METHODS

Binding test. The binding of functionalized nanoparticles to recombinant NRP-1 protein has been widely described previously by our group.[31] Reported values are the average of triplicate measurements.

Cell line, dark cytotoxicity. and photodynamic activity. To study the involvement of NRP-1, MDA-MB-231 breast cancer cells were used, strongly over-expressing NRP-1 receptor. Cell line and culture conditions have been described previously by our group.[31,24,25] Cell survival and photodynamic activity after incubation with the different batches of nanoparticles in the dark was measured using a 3-(4,5-dimethylthiazol-2-yl)-2,5-diphenyl tetrazolium bromide (MTT) assay as described previously.[31,35]

Animals and tumor model. All experiments were performed in accordance with animal care guidelines (Directive 2010/63/EU) and carried out by competent and authorized persons (personal authorization number 54-89 issued by the Department of Vetenary Services) in a registered establishment (establishment number C-54-547-03 issued by the Department of Vetenary Services). Male athymic nude rats (rnu-/rnu-) were used for this study (Harlan, Gannat, France). The rats were used for tumor implantation at age of 8 weeks (150-180 g).

During microsurgery (implantation or treatment protocol) and all acquisitions with microimaging, rats were anesthetized with a mixture of air and isoflurane concentrate (1.5-2% depending on the breathing) under sterile conditions. The rat was placed into a Kopf stereotactic frame (900M Kopf Instruments, Tujunga, CA). A midline incision was done and a burr hole was drilled 0.5 mm anterior and 2.7 mm lateral to the *bregma*. A skull anchor was fixed. 5.10^4 U87 cells were suspended in 5 µL Hank's Buffered Salt Solution (HBSS, 1X) and were injected in 4.4 mm into the brain parenchyma with a flow of 0.2 µL/min using a 10 µL Hamilton syringe. After injection, the scalp incision sutured (Suture 6.0 filament) and the surface was antiseptically cleaned.

Nanoparticles preparation for *in vivo* studies. Nanoparticles were suspended in ultrapure water and NaCl 9 $^0/_{00}$ (50:50) to obtain an equivalent concentration of 2.5 mM TPC or 200 mM Gd. Each batch of nanoparticles was buffered in order to obtain an iso-osmolar solution and pH 7.4 and conserved at 5°C. Injected TPC amounted to 1.75 µmol/kg as previously described.[27,28] The injection solution was prepared by dissolution in 9 $^0/_{00}$ NaCl to obtain an injection volume of 600 µL (*e.g.* 0.437 µmol of TPC or 84.2 µmol of Gd for a body weight of 250 g) and injected, following by 600 µL of 9 $^0/_{00}$ NaCl were injected during 1 min.

Inductively Coupled Plasma-Mass Spectroscopy. A Varian 820 MS instrument (Varian, Les Ulis, France) was used. All samples were completely dissolved with 70% HNO_3 and heated at 90°C until total mineralization. Each mineralized sample was solubilized in 25 mL of ultrapure water (resistivity >18.2 MΩ) and analyzed by ICP–MS (Laboratoire Environnement-Hygiène of ASCAL, Forbach, France). All removed samples were stored at -80°C prior to elemental analysis.

Nanoparticles biodistribution. MRI experiments were performed at 7 Tesla in a horizontal bore magnet (Bruker, Biospec, Ettlingen, Germany). Reference images ("Scout views") were first realized to obtain the brain position or abdominal position inside the magnet. 15 slices were obtained, 5 in each plan. ***For cerebral imaging***, a volume coil (internal diameter 72 mm) was used for radio frequency emission, and a surface coil was placed on the animal skull for the reception of the signal.

T2 weighted images. Coronal and horizontal T2 TurboRARE[36] (Rapid Acquisition with Relaxation Enhancement) spin echo sequence were performed to follow the tumor size.

T1 weighted images. Dynamic T1 weighted images were realized during the injection of the nanoparticles for characterization of the kinetics of the product inside the tumor by the "wash in" and "wash out".

For the abdominal imaging, a quadrature volume coil (inner diameter of 72 mm) was used for radio frequency emission and reception. Acquisitions were synchronized to the breath to prevent the kinetics blurring. The T1 weighted turboRARE[36] spin echo sequence was performed in coronal plan to characterize the clearance of the nanoparticles after injection.

MRI-guided iPDT and light delivery. Light delivery fiber was inserted through the skull anchor (Patent WO2012176050 A1) into the tumor tissue. The fiber tip (272 nm diameter, ULS 272, OFS, Norcross, U.S.A.) delivered the light (652 nm, 50 mW, 8 min 40 s, 26 J). A RARE T1 and T2 weighted imaging were performed before iPDT to control the positioning of the optical fiber inside the brain.

Perfusion MRI. Arterial Spin Labeling (ASL)[37] techniques were able to provide quantitative information about local tissue blood flow by observing the inflow of magnetically tagged arterial blood into imaging slice.

Magnetic resonance spectroscopy (MRS) analysis. A 1.7 mm cubic voxel was positioned in the glioma and in the striatum (controlateral side). Before the spectroscopic PRESS (Point-Resolved Spectroscopy Sequence) sequence acquisition a FastMAP[38] was performed in order to homogenise the magnetic field in the voxel.

PET-CT acquisition procedures. Metabolic brain imaging was performed by using a small animal PET-CT (MicroPET/CT INVEON, Siemens Preclinical Medical Solutions). The animal was deprived only from food 6 h prior to intravenous injection of [^{18}F]FDG. At 40 min after, the anesthetized animal was positioned on the scanner bed, which automatically moves inside the gantry of the CT scanner then further into the PET field of view, the acquisition protocol started. The CT scanner provided information with regards to tissue attenuation that is necessary for PET imaging accurate reconstruction. PET images were reconstructed with iterative algorithms of OSEM2D and corrected for attenuation and scatter. Imaging data analyses were performed on all frames by use of IRW (version 3.0) software.

Immunohistological analysis. Brain tissue was fixed during 10 days at room temperature in formol. Macro-samples of each brain (5 mm) were realized with a large rat coronal blocker (DKI-PA-001, David Kopf instruments, Phymep, Paris, France) and fixed still during 24 h. Samples were dehydrated in ethanol (96° followed by 100°). Histopathology was performed on 5 µm paraffined tissue sections. Hematoxylin, eosin and safran (HES) staining and Periodic-Acid-Schiff (PAS) were performed. Each section was pre-treated by EDTA (10 mM, pH:7.8) at 121°C during 3 h. To detect tumour cellular proliferation, sections were incubated for 1 night at room temperature with the primary antibody (rabbit monoclonal antibody anti-Ki67, 1:200 dilution buffer; SP6, RM-9106-S0, S1, NeoMarkers, Labvision). Glial fibrillary acidic protein (GFAP) was analysed using a mouse polyclonal antibody anti-GFAP (1:2000 dilution buffer, MS-280-P0, Thermo Fischer Scientific) and NRP-1 expression with a rabbit polyclonal antibody anti-NRP-1 (1:400 dilution buffer, Invitrogen Corporation, Camarillo, CA). $VEGF_{165}$ expression was detected with a rabbit polyclonal antibody anti-humanVEGF (1:100 dilution buffer, AB-2, PC-37, Oncogene Science, Inc., Cambridge, MA, USA). After washing, the slides were incubated for 1 h with the secondary goat polyclonal antibody anti-rat biotinylated IgG (1:400 dilution in PBS-Tween E0432, Dakocytomation, Denmark). The revelation of secondary biotinylated antibodies was performed with a streptavidin-horseradish peroxidase complex (1 h at room temperature, diluted 1:400 in PBS-Tween, Dakocytomation, Denmark) and the peroxidase substrate (5 min, Vector® NovoRedTM Substrate Kit for peroxydase, HistoGreen, Vector Laboratories, Paris). A hematoxylin counterstaining was performed to visualize the section by optical microscopy (AX-70 Provis, Olympus, Rungis, France).

Statistical analysis

Mann-Whitney U test was used to assess the significant level between independent variables. The level of significance was set to $p < 0.05$.

RESULTS

Nanoparticles characterizations: Photophysical and chemical properties, size distribution and zeta potential

The synthesis pathway has been previously described in Couleaud *et al.*, 2011.[31] **Figure S1** shows the photophysical and chemical characterization of nanoparticles. Absorption spectra

(**Fig. S1a**), fluorescence spectra (**Fig. S1b**) and $^1O_2$ luminescence spectra (**Fig. S1c**) in ethanol of free TPC and TPC grafted to nanoparticles. No significant changes in the quantum yields of fluorescence and $^1O_2$ production have been observed between free TPC and TPC grafted onto nanoparticles (**Fig. S1e**). Fluorescence of TPC (excitation and emission wavelengths at 420 and 600-800 nm, respectively) and fluorescence of tryptophan residues of ATWLPPR (excitation and emission wavelengths at 280 and 350 nm, respectively) have been used to quantify TPC and ATWLPPR grafted onto the nanoparticles. We found an average of 2 TPC molecules per nanoparticle and 4, 9 or 15 ATWLPPR peptides per nanoparticle depending on the amount we needed.[31] By measuring the partition coefficients of free TPC, NP-TPC, NP-TPC-ATWLPPR, we find that the formulation we developed have a higher hydrophilic character than the free TPC (**Fig. S1e**). DLS and HR-TEM measurements have permit to find a consistent diameter of 2.9±0.7nm and 2.8±0.2nm, respectively (**Fig. S1d**). The presence of ATWLPPR peptide on the surface of the NPs induces a significant decrease in the surface charge, as measured by zeta potential at pH 7.4 (**Fig. S1e**). As expected, the derivatization of the nanoparticles by DTPA rendered them water soluble in a wide pH range, including pH of biological fluid whereas the colloidal stability of uncoated nanoparticles was not sufficient.

Molecular affinity

As previously described, the endothelium-homing peptide ATWLPPR selectively targets NRP-1 receptor over expressed by neo-angiogenic vasculature.[23,24,26,27,28] ATWLPPR grafting onto nanoparticles was measured as previously described.[31] We tested different ATWLPPR grafting ratios onto nanoparticles: 4 peptides per nanoparticles (NP-TPC-ATWLPPR), 9 peptides per nanoparticle (NP-TPC-$(ATWLPPR)_9$) or 15 peptides per nanoparticle (NP-TPC-$(ATWLPPR)_{15}$). Molecular affinity of these functionalized nanoparticles to recombinant NRP-1 protein has been estimated using binding tests. As $VEGF_{165}$ binding to its receptors is heparin-dependent, the competitive binding experiments were always carried out in the presence of heparin. Nanoparticles conjugated to ATWLPPR indeed bound to recombinant NRP-1 chimeric protein (**Fig. 1a**). Interestingly, the best binding value was obtained with 4 peptides per nanoparticle with a decrease of the affinity related to the number of peptides (**Fig. 1a**). Binding of biotinylated $VEGF_{165}$ to NRP-1 was displaced by NP-TPC-ATWLPPR in a peptide concentration-dependent manner (IC_{50}=27 μM, **Fig. 1b**).

***In vitro* dark cytotoxicity without light exposure**

We used MDA-MB-231 breast cancer cells that strongly over-express NRP-1 receptor, as previously demonstrated[25]. MTT test was used to evaluate the dark cytotoxicity of the different batches of nanoparticles, control nanoparticles without TPC (NP), nanoparticles with TPC but without peptides (NP-TPC), and nanoparticles with 4 peptides (NP-TPC-ATWLPPR) for TPC concentrations ranging from 0.10 to 20.00 µM. A 24 h-incubation of MDA-MB-231 with nanoparticles in the absence of light exposure yielded a mean surviving cell fraction of more than 70% for concentrations up to 1.00 µM of TPC (**Fig. 1c**). All subsequent *in vitro* experiments were carried out at concentrations equal or inferior to 1.00 µM of TPC. At 10.00 µM of TPC, we can noticed that the presence of peptide units onto the nanoparticle increased significantly its cytotoxic effect probably due to an improved uptake but this effect was not verified for 20.00 µM concentration (**Fig. 1c**).

***In vitro* photodynamic activity after light treatment**

MDA-MB-231 cells were incubated with nanoparticles with TPC but without peptide NP-TPC and NP-TPC-ATWLPPR, and irradiated by 652 nm red light. Whereas NP-TPC at 0.1 µM displayed a weak photodynamic activity in MDA-MB-231 cells, conjugation with ATWLPPR significantly enhanced photodynamic efficiency (**Fig. 1d**). A statistically significant influence was also evaluated on the photodynamic activity for un-conjugated nanoparticles and peptides-functionalized nanoparticles with 1.00 µM of TPC using light doses from 5 to 20 J/cm^2 (**Fig. 1e**).

***In vivo* biodistribution and tumor tissue selectivity**

We followed the *in vivo* biodistribution of NP-TPC-ATWLPPR and NP-TPC nanoparticles 2 and 24 h post-intravenous injection. It appears that only the kidneys and the bladder, which are involved in renal excretion, showed a positive contrast enhancement of the MRI signal intensity (**Fig. 2a and 2b**). Similar biodistribution results were obtained for both un-conjugated and peptides-conjugated nanoparticles. Gadolinium concentration of each sample was measured by ICP-MS also demonstrating high levels in the kidneys 2 h after intravenous injection (**Fig. 2c**).

To investigate tumor tissue selectivity, we used U87 orthotopic model about 10 days after stereotatic implantation in nude rats. MRI analysis of the tumor tissue was investigated for un-conjugated and ATWLPPR- or LWRPTPA-targeted nanoparticles. LWRPTPA is a mix of aminoacids of ATWLPPR peptide without affinity for NRP-1 used as negative control. Just after intravenous injection, whatever the batches of nanoparticles the MRI signal intensity on

T1-weighted increased rapidly (**Supplementary Figure 3)**. According to time after intravenous injection of NP-TPC (**Fig. 3b**) and NP-TPC-$(LWRPTPA)_4$ (**Fig. 3c**) the curve profiles of the MRI signal intensity percentage were comparable with a marked difference between the ROIs corresponding to the total tumor tissue and the peripheral tumor tissue areas. However, for NP-TPC-ATWLPPR the kinetic profiles between MRI signal intensity percentage corresponding of the ROIs of the total tumor area and the peripheral tumor tissue appeared similar (**Fig. 3a**). These data reveal that the ATWLPPR targeted-nanoparticles can be delivered to the tumor site and that the presence of the ATWLPPR-targeting moiety provides a more selective contrast enhancement for the peripheral tumor tissue. As illustrated in the respective inserts of the **figure 3d**, the tumor periphery was not delimited by a margin of connective tissue conversely MRI images from NP-TPC and NP-TPC-$(LWRPTPA)_4$ appeared were well demarcated.

In order to complete these investigations and to understand the tropism of NP-TPC-ATWLPPR for the tumor tissue periphery, we performed dynamic contrast-enhanced perfusion MRI and as expected, we clearly visualized that the margins of the tumor volume were more vascularized than its center (**Fig. 4a**). Vascular phenotype in angiogenic vessels was characterized by an over expression of NRP-1 protein mainly in this peripheral interest area (**Fig. 4b**); the margins of the tumor tissue were more vascularized and the neoangiogenic vessels from the peripheral interest area between the tumor tissue and the brain adjacent to tumor expressed NRP-1 protein. It appears that ATWLPPR-conjugated nanoparticles target vessels mainly located in the peripheral tumor tissue with an angiogenic phenotype.

***In vivo* interstitial stereotactic PDT by interventional MRI**

Tumors tissue, visualized by T1-weighted imaging after injection of nanoparticles, was illuminated *via* an optical fiber placed stereotactically into the brain of each animal. The fiber position was confirmed by another coronal T1-weighted MRI acquisition (**Fig. 5a**) and visualized by a colocalization between MRI combined with PET-CT images **(Fig. 5a, left pictures**) Patent WO2012176050 A1. Brain tumor tissue was illuminated about 1 h post-injection with nanoparticles, taking into account the drug-light interval according to the MRI signal intensity.

Following iPDT using these ultrasmall nanoplatforms, advanced imaging complementary techniques (perfusion MRI, proton MRS, PET-CT) were applied as a proof of concept study.

Before and immediately after iPDT, cerebral perfusion MRI was realized for each treated animal (**Fig. 5b**). Top and bottom of the **figure 5b** show the tumor perfusion images.

The tumor perfusion images have been obtained for two animals and they illustrate clearly that the intratumoral blood perfusion significantly decreased for tumors treated with both batches of nanoparticles. The most interesting point is that blood perfusion declined for more than 80% mean of the initial values only for tumors treated with NP-TPC-ATWLPPR.

Magnetic resonance spectroscopy acquisition in tumor was performed to quantify intratumoral metabolites, using creatine as reference. Proton MRS provides a noninvasive method for evaluating some metabolic components. Because this technique measures the presence of specific metabolites, it is independent of anatomic information and may be used to characterize lesions. Metabolites over-expressed 24 h after iPDT were listed in the **figure 5c** as metabolites/creatine ratios. After iPDT for tumors treated by NP-TPC-ATWLPPR, CH_2/creatine and CH_3/creatine lipids ratios related to the tumor cells necrosis, increased by a factor of 3.3 and 3.0, respectively. Changes in the concentrations of choline-containing metabolites have been implicated in both cell proliferation and death processes. An increase of 1.9- and 2.1-fold of choline/creatine ratios was measured after treatment for NP-TPC-ATWLPPR and NP-TPC, respectively.

In order to estimate tumor tissue metabolism, sample images were performed 4 and 6 days after treatment using a combination of PET-CT imaging technology. This modality allowed intra tumor metabolism detection after incorporation of [^{18}F]FDG by cells. The uptake of [^{18}F]FDG in tumor tissue and in surrounding healthy tissue is time-dependent. [^{18}F]FDG uptake reflects tumor physiology, tumor cell density, and blood supply (**Fig. 6**). Using non-conjugated nanoparticles, the percentage of injected [^{18}F]FDG dose increased from 1.40 (just before iPDT) to 1.80 (four days after iPDT) and to 1.70 (six days after treatment). At the same times, NP-TPC-ATWLPPR-treated tumor also described an increase related to time post-treatment in percentage of injected dose with 1.40 before treatment followed by 1.53 and 1.92, four and six days after treatment, respectively. The calculated values of the tumor metabolism after non-conjugated nanoparticles treatment were 0.040±0.002 and 0.023±0.002 for 1 mm^3 of tumor tissue, two days and six days post-iPDT, respectively. For conjugated nanoparticles treatment, the calculated values were 0.028±0.001 and 0.021±0.001 for 1 mm^3 of tumor tissue, 2 days and 6 days post-iPDT, respectively.

Histological examination of tissue sections taken from brain tissue immediately after iPDT indicated a vascular disruption and oedema into both tumor and BAT areas (**Fig. 7a**). The alteration of the extra cellular matrix after treatment was suggested by a decrease in PAS protein expression (**Fig. 7b**). An extensive and distinct staining for Ki67 and VEGF was observed in the tumor tissue before treatment followed by an intense decrease of these

proteins expression immediately after iPDT (**Fig. 7c and d**). All these results obtained by imaging techniques and histological analysis confirm that using this stereotactic iPDT protocol the selected nanoplatforms induce an *in vivo* photodynamic activity.

DISCUSSION

Kopelman *et al.* were the first to describe targeted nanoplatforms combining both MRI and PDT agents. They described a nanoplatform based on PAA (polyacrylamid acid)-modified core of iron oxide, coupled to the RGD peptide.[39,40] Several potent small-molecule $\alpha_v\beta_3$ antagonist-based RGD compounds have been studied under clinical trials for anti-angiogenesis, drug delivery, and cancer imaging. The promising results have highly suggested that integrin receptors are important targets for molecular imaging, drug delivery and therapy. Recently, another team grafted an anti-HER2 antibody onto gold nanoparticles.[41] Human Epidermal Growth Factor Receptor-2 (HER2) belongs to the HER family involved in intracellular signaling mechanisms including cell proliferation. By coupling the anti-HER2 to nanoparticles, Stuchinskaya *et al.* demonstrated *in vitro* a selective targeting in cells overexpressing HER2 and a photodynamic effect related to the expression of HER2. F3 peptide has also been coupled to nanoparticles to target tumor vasculature. This peptide is an N-terminal fragment (amino acid sequence 17-48) of the high human protein 2 (HMGN2) mobility group.[42] It is expressed in the nuclei of tumor and endothelial cells, including MDA-MB-435 tumor cells. *In vivo*, in a model of orthotopic glioma, polyacrilamide F3-conjugated nanoparticles containing photofrin led to a photodynamic efficiency.[43] F3 peptide was also grafted onto polyacrilamide nanoparticles encapsulated methylene blue.[44,45] Only a very limited number of studies have been performed to actively target tumor vascular endothelial cells.[46,47]

Our strategy aims to favor the vascular effect of PDT by targeting tumor-associated vascularization. Our preliminary approach consisted to the conjugation of a chlorin to a heptapeptide ATWLPPR targeting NRP-1, over-expressed by tumor angiogenic vessels.[23,24,26,27,28,31] This conjugated-chlorin proved to be very efficient *in vitro* in human umbilical vein endothelial cells compared to its non-conjugated form.[23] In this study, in order to check the absence of dark cytotoxicity of the different batches of nanoparticles and to assess the impact of the uptake improvement on the photodynamic efficiency according to the nanoparticles grafting level, MDA-MB-231 cells were selected. As previously demonstrated, this cell line strongly over-express NRP-1 receptor, leading us to evidence a statistically significant decrease of the conjugated photosensitizer cellular uptake after RNA interference-

mediated silencing of NRP-1.[24] Here, we designed ultrasmall ATWLPPR-targeted silica-based nanoparticles encapsulated gadolinium oxide as MRI contrast agent and a chlorin as photosensitizer. We previously described the *in vitro* photodynamic efficiency of multifunctional silica-based nanoparticles for PDT.[31] In this study, we demonstrated that nanoparticles conjugated to ATWLPPR bound to recombinant NRP-1 chimeric protein and interestingly, the best binding value was evidenced with four peptides per nanoparticle with a decrease of the affinity related to the number of peptides. Binding of biotinylated $VEGF_{165}$ to NRP-1 was displaced by NP-TPC-ATWLPPR in a peptide concentration-dependent manner. This decrease of affinity related to the number of grafted peptides maybe related to the steric hindrance due to the number of peptide units in comparison with the ultra-small size of the nano-object. By *in vitro* experiments with MDA-MB-231 cells over-expressing NRP-1, we also observed that the presence of peptide units onto the nanoparticle increased significantly its cytotoxic effect probably due to an improved cellular uptake. Moreover, we demonstrated that nanoparticles conferred photosensitivity to cells, providing evidence that the chlorin molecules grafted within the nanoparticle matrix can be photoactivated to yield photocytotoxic effects *in vitro* but also *in vivo*.

For the first time, we evidenced the *in vivo* tropism of ATWLPPR-conjugated nanoparticles targeting NRP-1 receptor for the peripheral tumor tissue. Indeed, after intravenous injection of non-conjugated nanoparticles when we selected a ROI corresponding to the total tumor tissue area, we only observed the Enhanced Permeability and Retention (EPR) effect.[48,49] Leaky fenestration caused extravasations of non-conjugated nanoparticles out of the vasculature. Due to an inefficient lymphatic drainage, there was a poor clearance of the nanoparticles into the interstitial space of the tumor tissue. In contrast after intravenous injection of ATWLPPR-conjugated nanoparticles, they provided a more selective contrast enhancement for angiogenic endothelial cells that line the neovessels mainly located in the peripheral tumor and over expressing NRP-1. Results from perfusion MRI argue that the margins of the tumor were more vascularized. Using ATWLPPR-targeted nanoplatforms, the positive contrast enhancement of the tumor by MRI, allowed us to visualize the proliferating part of the tumor tissue, which was not the case with unconjugated nanoparticles.

The average size of these nanoparticles makes them amenable to renal clearance and to avoid retention. Three hours after intravenous injection less than 0.2% of the injected nanoparticles are in organs other than kidneys and bladder[50] and the uptake into different brain tumor models (U87 and 9L) was demonstrated to be sufficient to perform MRI imaging.[51] After intravenous injection of the nanoparticles (with or without peptide), the

positive contrast enhancement of the tumor tissue by MRI allowed us to optimize the optical fiber implantation. With ^{1}H-MRS, we applied the quantitative spectral analysis, allowing us to measure and to compare metabolites expression before and after iPDT for tumor and controlateral hemisphere. Lehtimaki et *al.* used BT4C tumors underdoing (ganciclovir-HSV-tk) gene therapy as a model of programmed cell death.[52] They characterized metabolic changes associated with programmed cell death, most notably a large increase in polyunsaturated and saturated fatty acids. As explained by Hakumaki and *al.*, saturated and polyunsaturated lipids concentration extensively increases during programmed cell death despite severe cell loss.[53] In our study, water-suppressed ^{1}H NMR spectra from U87 *in vivo* are dominated by strong lipids signals arising from a $-CH_2CH_2CH_2-$ of saturated lipids and a $-CH_2CH_3-$ of satured lipids. Moreover, these peaks intensity increase ~2 folds after treatment. Choline-containing metabolites (choline, phosphocholin, glycophosphocholin, taurine, myo-inositol) decreased at an advanced stage of apoptotic cell death.[54] Choline-containing metabolites level increased after treatment, suggesting a presence of an acute tumor inflammatory response. In patients at the very early stage of multiple sclerosis with acute inflammatory processes, choline-containing metabolites increased with the decrease in *N*-acetyl aspartate levels.[55] It is also well known that PDT induced inflammatory response.[57] Moreover, localized oedema was observed just after treatment by histological analysis. This inflammatory reaction may be secondary to an ischemic-related cell death and cytokines production. We previously demonstrated that tumors treated with the peptide-conjugated photosensitizer showed an increase in TNF-α and IL-6 protein levels.[28] PDT-induced inflammatory changes were widely characterized by enhanced expression of a number of pro-inflammatory cytokines, including IL-1β, TNF-α and IL-6.[56,57] Using the peptide-conjugated photosensitizer, we demonstrated an induction of tissue factor expression immediately post-treatment, leading to the establishment of thrombogenic effects within the vessel *lumen*[28]. Tissue factor pathway can also influence inflammatory signaling by activation of protease-activated receptor-1 and -2 or expression of TNF-α and IL-6.[58] Szotowski et *al.* explained that asHTF (alternatively spliced human tissue factor) released from endothelial cells contributes to the creation of an imbalance in hemostasis. This soluble tissue isoform released from endothelial cells in response to inflammatory cytokines becomes pro-coagulant in presence of phospholipids.[28,58]

After iPDT, non-invasive imaging approaches and histological examination indicated a vascular disruption and oedema into both tumor and BAT areas using NP-TPC-ATWLPPR.

Even if it is well known that inflammatory response contributes to *in vivo* PDT efficiency, these effects may increase the risk for a compression syndrome. Our finality is currently to follow the tumor response to the iPDT by non-invasive imaging monitoring that could give warning signs before the tumor regrowth and thus, could provide a base for a rational approach to determine a schedule of irradiation. A judicious choice of iPDT regimens could minimize inflammatory responses. Specific dosimetry for PDT is challenging owing to the nonlinear interaction between light dose, irradiation time, and concentration of both the photosensitizer and molecular oxygen.[59,60] The effect of PDT on any tumor is dependent on a number of factors. These include the light energy absorbed by the target tumor tissue, the concentration of the photosensitizer in the tumor tissue, and the inherent sensitivity of the tissue to the photodynamic effect. The dose delivered during iPDT is determined by the amount of reactive oxygen species (ROS) that are generated, itself dependent on the photosensitizer, its concentration, the local fluence and the availability of oxygen. Tissue hypoxia resulting from vascular damage is also a continual source of ROS production. Further, pro-inflammatory cytokines and growth factors greatly increase intracellular ROS generation. A combination of both explicit and implicit parameters, monitored during iPDT would be valuable tools

These nanoparticles provide interesting possibilities for new avenues to significantly improve iPDT. For example, the traditional delay between photosensitizer administration and light exposure needed to allow for enough clearance from normal adjacent tissue to occur along with prolonged cutaneous photosensitization are well-known disadvantages of PDT. However, these disadvantages were not observed in the application in this study involving a covalently grafted photosensitizer in nanoparticles. These nanoparticles were produced to contain both a magnetic resonance contrast agent along with a therapeutic agent. The ability of vascular targeting along with imaging capability while carrying a payload of a drug by these nanoparticles proves for a multifunctional nanoparticle technology that can be adapted for other therapeutic purposes in future studies.

Legends

Figure 1. Molecular affinity of nanoparticles with peptides, *in vitro* dark cytotoxicity and photodynamic activity. Binding of NP-TPC-ATWLPPR (black), NP-TPC-$(ATWLPPR)_9$, (dark grey) and NP-TPC-$(ATWLPPR)_{15}$ (clear grey) to recombinant NRP-1 protein compared to nanoparticles without ATWLPPR (**a**). Binding of biotinylated $VEGF_{165}$ (5 ng/mL; 110 pM) to NRP-1 in the presence of 2 µg/mL heparin was evaluated when increasing concentrations of nanoparticles were added (data points show the mean ± SD, n=3). Binding curve of nanoparticles with 4 peptides (NP-TPC-ATWLPPR to recombinant NRP-1 protein (EC_{50}=27µM) (data points show the mean ± SD, n=3) (**b**). Dark cytotoxicity and photodynamic therapy sensitivity to different formulations: NP-TPC-ATWLPPR (black), NP-TPC (dark grey) and control NP (without TPC nor peptide in white) in MDA-MB-231 cells depending on nanoparticles concentration, as determined by MTT test (data points show the mean ± SD, n=6) (**c**). Measurements of photosensitivity of MDA-MB-231 cells to NP-TPC (black) and NP-TPC-ATWLPPR (grey) (corrected by respective nanoparticles in dark cytotoxicity) (**d-e**). Survival was obtained for cells incubated with different concentrations of nanoparticles for 24 h before exposure to doses of light from 1 to 20 J/cm² at 0.1 µM of TPC (**d**) and at 1 µM of TPC (**e**) by MTT test (data points show the mean ± SD, n=6).

Figure 2. Abdominal biodistribution visualized with dynamic T1 weighted images acquisition 2 or 24 h after intravenous injection (84.2 µmol of Gd for a body weight of 250 g) in the caudal vein of hybrid gadolinium oxide nanoparticles with NP-TPC-ATWLPPR (**a**), NP-TPC (**b**). The parameters of the sequence were: TR/TE = 400 / 9 ms, 80 mm square FOV, matrix 256 x 256. 16 slices of 1.5 mm without interslice gap allowed detecting nanoparticles in kidneys and bladder. For both nanoparticle types, a positive MRI signal appeared in the kidneys and the bladder. Gadolinium concentrations were evaluated in each organ for different nanoparticles (**c**). K: kidneys; B: bladder; L: liver.

Figure 3. Cerebral biodistribution and tumor tissue tumor selectivity of gadolinium oxide nanoparticles with peptide (ATWLPPR or LWRPTPA) or without peptide visualized during 1 h and, immediately after intravenous injection (84.2 µmol of Gd for a body weight of 250 g). Dynamic T1 weighted images acquisition was started before the injection of the nanoparticles to characterize the kinetics of the product inside the tumor. This sequence was a FLASH[61] (Fast Low-Angle SHot) sequence, which was set to obtain a temporal resolution of one image

per 19 s. The parameters were: TR/TE = 200 /2.4 ms, matrix size of 128 x 128 pixels, a 40 mm square FOV. MRI signal intensity curves of NP-TPC-ATWLPPR (**a**), NP-TPC (**b**) and NP-TPC-LWRPTPA (**c**). All curves represent acquisitions selected from different regions of interest (ROI): ■ Controlateral healthy hemisphere, ■ Peripheral tumor tissue and ■ Total tumor tissue. T1 coronal MRI images obtained (1) before nanoparticles intravenous injection, (2) several seconds after injection, (3) maximal MRI signal intensity after injection and (4) 1h post-injection (**d**).

Figure 4. Perfusion MRI was done with ASL method by using EPI[62] (Echo Planar Imaging) FAIR[63] (Flow-sensitive Alternating Inversion Recovery) sequence with the parameters: TR/TE = 18000 / 13.5 ms, 22 TI (Inversion Time) from 26 ms to 2126 ms, 40 mm square FOV, matrix size, 64 x 80 pixels. Tissue perfusion was measured on a single axial slice of 0.85 mm focused on the tumor. The acquisition time was 26 min. Enlarged view of the corresponding hyperperfusion zone of the peripheriral tumor tissue **(a)**. Tissue perfusion was measured on a single axial slice of 0.85 mm focused on the glioma 10 days after graft. (T: tumor; V: vessels; BAT: brain adjacent to tumor). Representative images of NRP-1 staining in red counterstained with haematoxylin (blue) obtained from tumor sections of the U87 tumors. Enlarged view of the corresponding specimen **(b)**. NRP-1 protein was highly expressed by endothelial cells in peripheral tumor and lowly by astrocytoma cells.

Figure 5. (a) A RARE T1 and T2 weighted imaging performed before iPDT to control the positioning of the optical fiber inside the brain. Volume coil was used during the acquisition. Coronal T1 TurboRARE spin echo sequences were performed before and after nanoparticles injection. The parameters were: TR/TE = 400/9 ms, matrix size 256 x256 pixels, FOV, 40 x 40 mm, Slice geometry was the same as the T2 weighted images. Time acquisition of each T1 weighted sequence was 2.30 min. Longitudinal segmentation of the brain *via* MRI and CT scan, showing the stereotactic interstitial implantation of the optical fiber using an anchor (**a**). Perfusion MRI immediately before (up) and after iPDT (down) using nanoparticles NP-TPC-ATWLPPR and NP-TPC (EPI FAIR sequence, TR/TE = 18000 / 13.5 ms, 22 TI from 26 ms to 2126 ms). Tissue perfusion was measured on a single axial slice of 0.85 mm focused on the glioma (**b**). MRS results before and 24 h after iPDT using nanoparticles NP-TPC-ATWLPPR and NP-TPC. The parameters of the PRESS[64] sequences were: TR/TE = 2500 / 20 ms, Nex = 512, time acquisition = 22 min. The spectroscopic data was post-treated on Topspin 2.0 (Bruker, Germany) (**c**).

Figure 6. Fusion of horizontal images from MRI, PET and CT before, four and six days after iPDT using NP-TPC-ATWLPPR. The parameters of sequence T2 weighted imaging were: TR /TE = 5000 / 77 ms, matrix size 256 x 256 pixels, field of view (FOV), 40 x 40 mm. For coronal images, 18 slices of 0.5 mm without an intersection gap, and 20 slices of 0.85 mm for axial images were acquired. The acquisition time for each sequence was 5.20 min. For PET, the radiotracer used is the fluorine-18 labeled fluoro-2-deoxyglucose and referred to as [^{18}F]FDG (average dose ~37 MBq (1 mCi), in 0.5 mL of saline). The CT imaging parameters were the following: X-ray voltage: 80 kVp; anode current: 500 mA; exposure time of 280 milliseconds of each of the 180 rotational steps. Using a summed image of the last 3 frames, ROIs were manually drawn on multiple planes to obtain volumetric ROIs of the whole brain, the tumor, the mirror region to the tumor, the cerebellum and an external background region. Statistical analyses were performed to compare regional cerebral metabolism of the same rat at pre-treatment scan and at post treatment scan. Similar analyses were performed with metabolic relative ratios normalized to cerebellum activity.

Figure 7. Histological images of U87 tumor and BAT before (left) and immediately after iPDT (right) using NP-TPC-ATWLPPR. After treatment, representative oedema images of hematoxylin-eosin-safran staining obtained from brain section in glioma compared to before treatment (**a**). Representative images of PAS staining (**b**) and Ki67 staining counterstained with haematoxylin (**c**). VEGF staining counterstained with haematoxylin (**d**) highly expressed in BAT before iPDT and unexpressed immediately after iPDT. (BAT: brain adjacent to tumor; O: oedema; T: tumor; V: vessels).

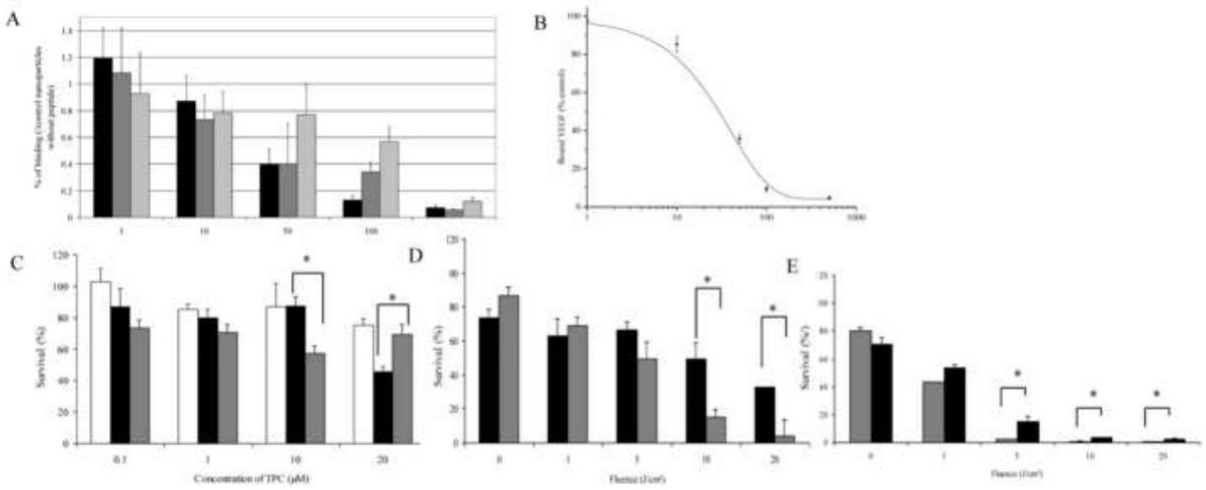

Figure 1

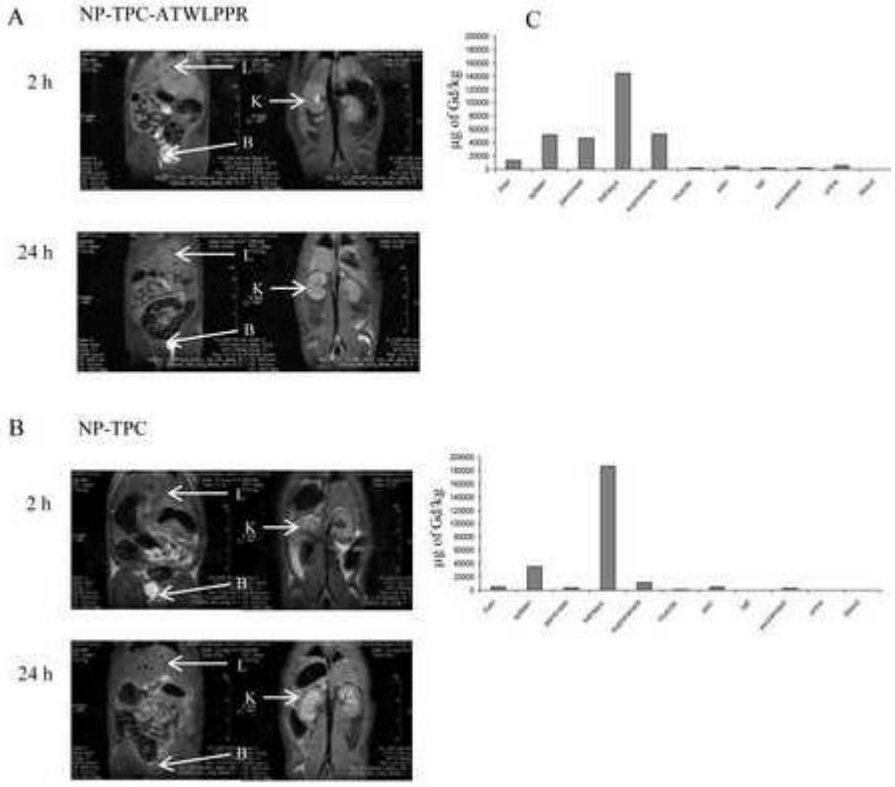

Figure 2

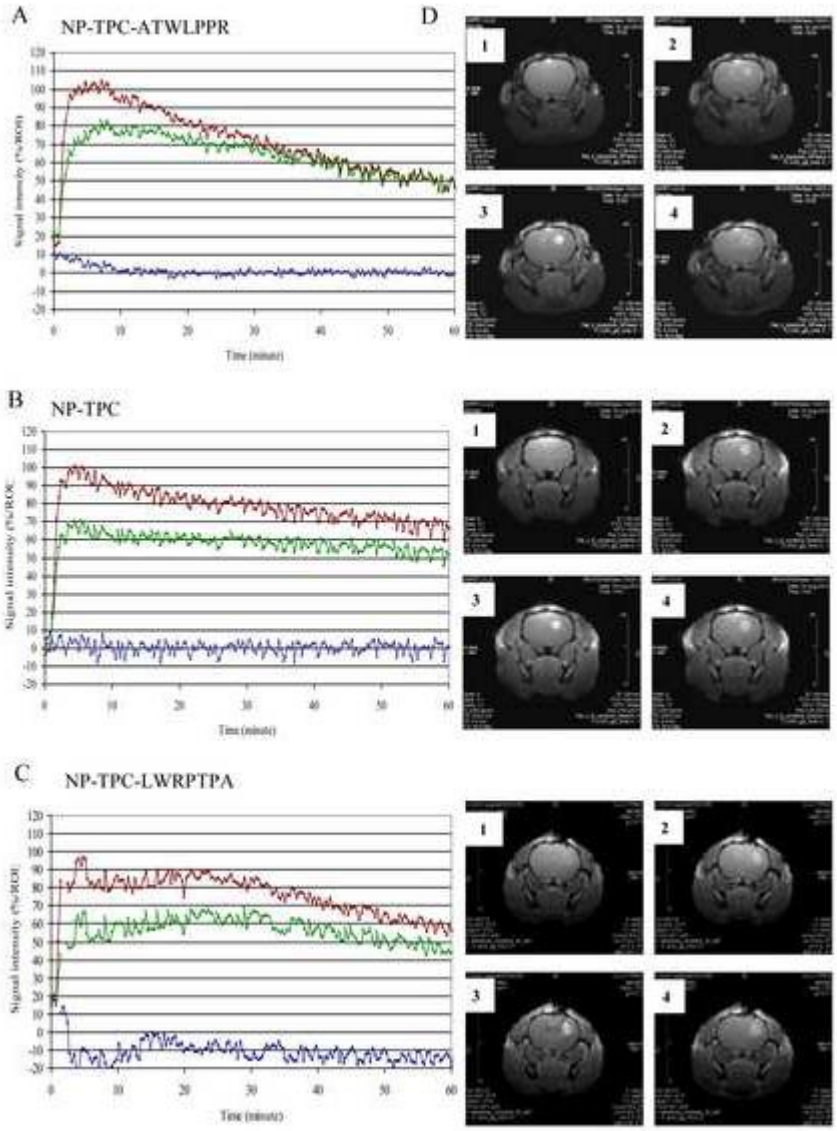

Figure 3

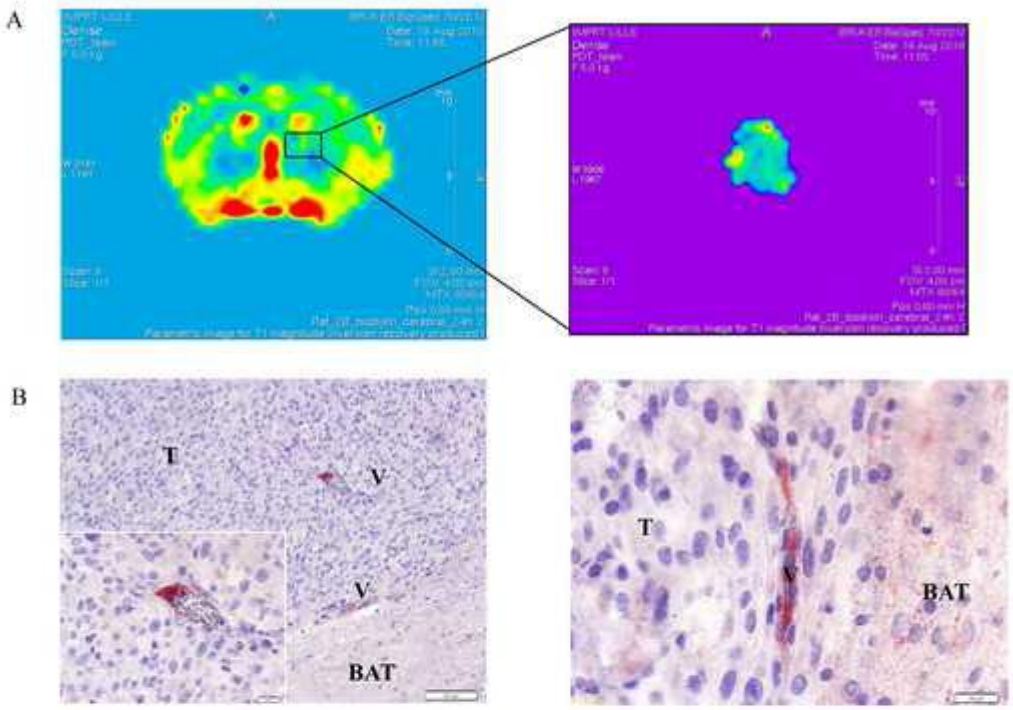

Figure 4

A

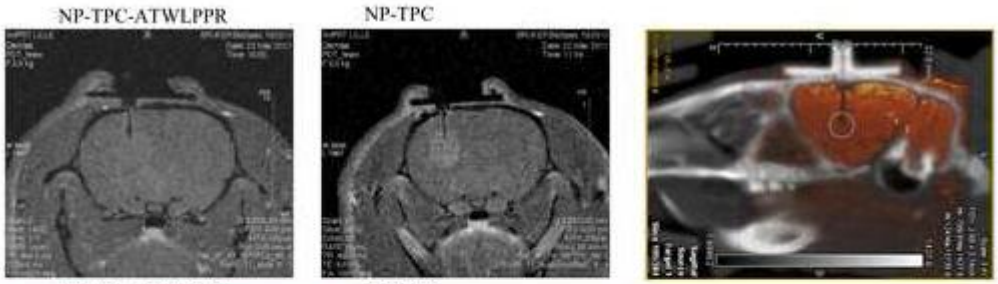

B

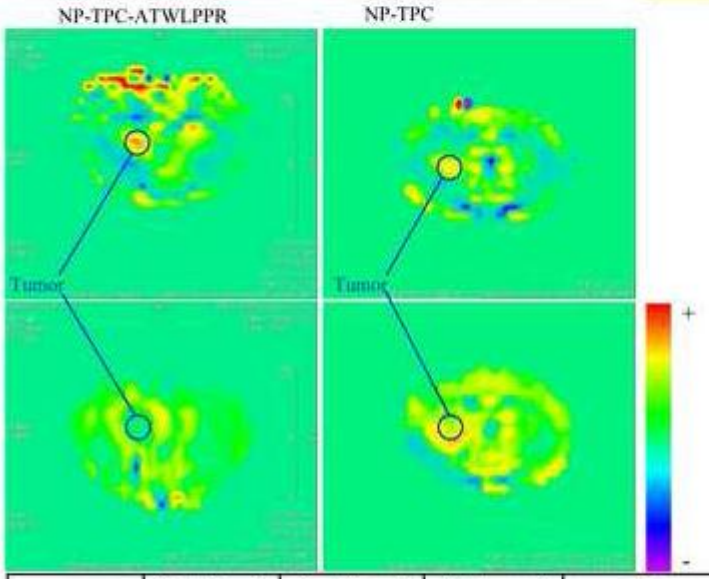

C

Ratio	Controlateral brain before iPDT*	Controlateral brain 24 h after iPDT*	Intratumoral before iPDT*	Intratumoral 24 h after iPDT**	
				NP-TPC-ATWLPPR	NP-TPC
CH3/crea	0.75±0.24	0.84±0.35	1.70±0.08	**5.17**	**3.17**
CH2/crea	0.61 ±0.18	**2.81±0.55**	3.30±0.33	**11.02**	**9.99**
N-acetyl aspartate/crea	1.08 ±0.23	0.90±0.23	0.99 ±0.41	1.28	1.81
Choline/crea	0.88 ±0.12	**1.41±0.59**	3.32 ±0.75	**6.41**	**6.95**
Lactate/crea	0.54 ±0.11	0.70 ±0.45	2.07 ±1.49	**3.11**	**3.14**
Myo-inositol/crea	0.25 ±0.07	0.37±0.10	1.04 ±0.54	**1.71**	**2.65**
Glutamate/ crea	0.33 ±0.13	0.52±0.19	0.88 ±0.17	1.16	1.03
Taurine/crea	0.37 ±0.09	0.68±0.32	0.38 ±0.2	1.71	0.48

* Average ± S.D., n=3; ** one sample analyzed

Figure 5

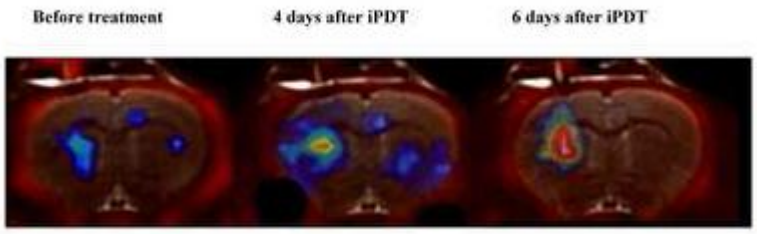

Figure 6

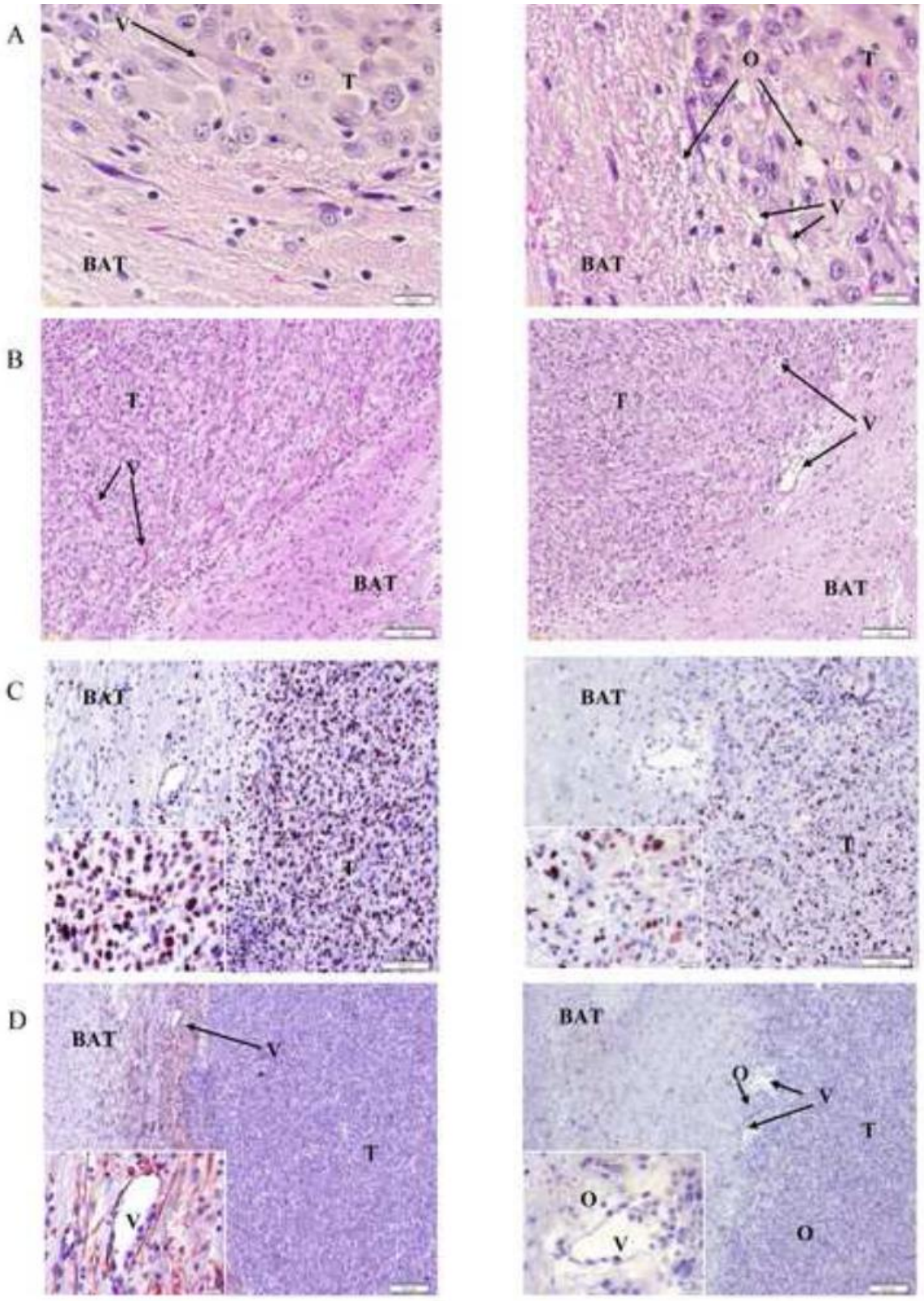

Figure 7

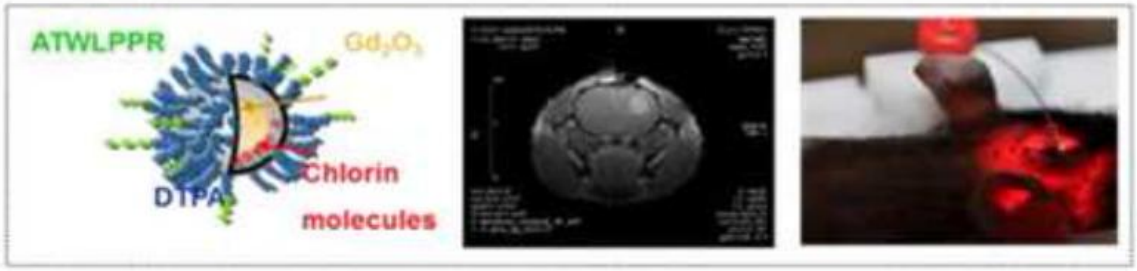

Graphical Abstract

MULTIFUNCTIONAL ULTRASMALL NANOPLATFORMS FOR VASCULAR-TARGETED INTERSTITIAL PHOTODYNAMIC THERAPY OF BRAIN TUMORS GUIDED BY REAL-TIME MRI

Denise Bechet, Florent Auger, Pierre Couleaud, Eric Marty, Laura Ravasi, Nicolas Durieux, Corinne Bonnet, François Plénat, Céline Frochot, Serge Mordon, Olivier Tillement, Régis Vanderesse, François Lux, Pascal Perriat, François Guillemin, Muriel Barberi-Heyob

This study is the first *in vivo* proof of concept of closed-head interstitial photodynamic therapy guided by real-time MRI using targeted ultrasmall nanoplatforms. After treatment, non-invasive imaging approaches and histological examination indicated a vascular disruption and oedema into the tumor tissue areas using the conjugated nanoparticles.

Bibliography

1 Beck TJ, Kreth FW, Beyer W, Mehrkens JH, Obermeier A, Stepp H, et al. Interstitial photodynamic therapy of nonresectable malignant glioma recurrences using 5-aminolevulinic acid induced protoporphyrin IX. Lasers Surg. Med. 2007;**39**:386-393.

2 Krishnamurthy S, Powers SK, Witmer P, Brown T. Optimal light dose for interstitial photodynamic therapy in treatment for malignant brain tumors. Lasers Surg. Med. 2000;**27**:224-234.

3 Stummer W, Beck T, Beyer W, Mehrkens JH, Obermeier A, Etminan N, et al. Long-sustaining response in a patient with non-resectable, distant recurrence of glioblastoma multiforme treated by interstitial photodynamic therapy using 5-ALA: case report. J Neurooncol 2008;**87**:103-109.

4 Kostron H, Fiegele T, Akatuna, E. Combination of FOSCAN® mediated fluorescence guided resection and photodynamic treatment as new therapeutic concept for malignant brain tumors. Medical Laser Application 2006;**21**:285-290.

5 Stepp H, Stepp H, Beck T, Pongratz T, Meinel T, Kreth FW, et al. ALA and malignant glioma: fluorescence-guided resection and photodynamic treatment. J Environ Pathol Toxicol Oncol 2007; 26:157-164.

6 Eljamel MS, Goodman C, Moseley H. ALA and Photofrin fluorescence-guided resection and repetitive PDT in glioblastoma multiforme: a single centre Phase III randomised controlled trial. Lasers Med Sci 2008;**23**:361-367.

7 Zilidis G, Aziz, F, Telara, S, Eljamel MS. Fluorescence image-guided surgery and repetitive Photodynamic Therapy in brain metastatic malignant melanoma. Photodiagnosis Photodyn Ther 2008;**5**:264-276.

8 Aziz F, Telara S, Moseley H, Goodman C, Manthri P, Eljamel MS. Aziz F, et al. Photodynamic therapy adjuvant to surgery in metastatic carcinoma in brain. Photodiagnosis Photodyn Ther 2009; **6**:227-230.

9 Johansson A, Palte G, Schnell O, Tonn JC, Herms J, Stepp H, et al. 5-Aminolevulinic acid-induced protoporphyrin IX levels in tissue of human malignant brain tumors. Photochem Photobiol 2010;**86**:1373-1378.

10 Jiang F, Robin AM, Katakowski M, Tong L, Espiritu M, Singh G, Jiang F, et al. Photodynamic therapy with photofrin in combination with Buthionine Sulfoximine (BSO) of human glioma in the nude rat. Lasers Med Sci 2003;**18**:128-133.

11 Stummer W, Pichlmeier U, Meinel T, Wiestler OD, Zanella F, Reulen HJ. ALA-Glioma Study Group. Fluorescence-guided surgery with 5-aminolevulinic acid for resection of malignant glioma: a randomised controlled multicentre phase III trial. Lancet Oncol 2006;**7**:392-401.

12 Zimmermann A, Ritsch-Marte M. Kostron. H. mTHPC-mediated photodynamic diagnosis of malignant brain tumors. Photochem Photobiol 2001;**74**:611-616.
13 Folkman, J. Angiogenesis in cancer, vascular, rheumatoid and other disease. Nat Med. 1995;**1**:27-31.
14 Dougherty TJ, Gomer CJ, Henderson BW, Jori G, Kessel D, Korbelik M, et al. Photodynamic therapy. J Natl Cancer Inst 1998;**90**:889-905.
15 Ichikawa K, Hikita T, Maeda N, Yonezawa S, Takeuchi Y, Asai T, et al. Antiangiogenic photodynamic therapy (PDT) by using long-circulating liposomes modified with peptide specific to angiogenic vessels. Biochim Biophys Acta 2005;**1669**:69-74.
16 Chen B, Pogue BW, Luna JM, Hardman RL, Hoopes PJ, Hasan T, et al. Tumor vascular permeabilization by vascular-targeting photosensitization: effects, mechanism, and therapeutic implications. Clin Cancer Res 2006;**12**:917-923.
17 Fingar VH, Taber SW, Haydon PS, Harrison LT, Kempf SJ, Wieman TJ, et al. Vascular damage after photodynamic therapy of solid tumors: a view and comparison of effect in pre-clinical and clinical models at the University of Louisville. In Vivo 2000;**14**:93-100.
18 Huang Z, Chen Q, Luck D, Beckers J, Wilson BC, Trncic N, et al. Studies of a vascular-acting photosensitizer, Pd-bacteriopheophorbide (Tookad), in normal canine prostate and spontaneous canine prostate cancer. Lasers Surg Med 2005;**36**:390-397.
19 McMahon KS, Wieman TJ, Moore PH, Fingar VH. Effects of photodynamic therapy using mono-L-aspartyl chlorin e6 on vessel constriction, vessel leakage, and tumor response. Cancer Res 1994;**54**:5374-5379.
20 Wieman TJ, Mang TS, Fingar VH, Hill TG, Reed MW, Corey TS, Wieman TJ, et al. Effect of photodynamic therapy on blood flow in normal and tumor vessels. Surgery 1998;**104**:512-517.
21 Fingar VH, Wieman TJ, Wiehle SA, Cerrito PB. The role of microvascular damage in photodynamic therapy: the effect of treatment on vessel constriction, permeability, and leukocyte adhesion. Cancer Res 1992;**52**:4914-4921.
22 Starzec A, Ladam P, Vassy R, Badache S, Bouchemal N, Navaza A, Starzec A, et al. Structure-function analysis of the antiangiogenic ATWLPPR peptide inhibiting VEGF(165) binding to neuropilin-1 and molecular dynamics simulations of the ATWLPPR/neuropilin-1 complex. Peptides 2007;**28**:2397-2402.
23 Tirand L, Frochot C, Vanderesse R, Thomas N, Trinquet E, Pinel S, Tirand L, et al. A peptide competing with VEGF165 binding on neuropilin-1 mediates targeting of a chlorin-type photosensitizer and potentiates its photodynamic activity in human endothelial cells. J Control Release 2006;**111**:153-164.
24 Thomas N, Pernot M, Vanderesse R, Becuwe P, Kamarulzaman E, Da Silva D, François A, Frochot C, Guillemin F, Barberi-Heyob M. Photodynamic therapy targeting neuropilin-1: Interest of pseudopeptides with improved stability properties. Biochem Pharmacol 2010;80:226-235. e
i

25 Tirand L, Thomas N, Dodeller M, Dumas D, Frochot C, Maunit B, et al. Metabolic profile of a peptide-conjugated chlorin-type photosensitizer targeting neuropilin-1: an in vivo and in vitro study. Drug Metab Dispos 2007;**35**:806-813.
26 Thomas N, Tirand L, Chatelut E, Plénat F, Frochot C, Dodeller M, et al. Tissue distribution and pharmacokinetics of an ATWLPPR-conjugated chlorin-type photosensitizer targeting neuropilin-1 in glioma-bearing nude mice. Photochem Photobiol Sci 2008;**7**:433-441.
27 Tirand L, Bastogne T, Bechet D, Linder M, Thomas N, Frochot C, et al. Response Surface Methodology: An Extensive Potential to Optimize in vivo Photodynamic Therapy Conditions. Int J Radiat Oncol Biol Phys 2009;**75**:244-252.
28 Bechet D, Tirand L, Faivre B, Plénat F, Bonnet C, Bastogne T, et al. Neuropilin-1 Targeting Photosensitization-Induced Early Stages of Thrombosis via Tissue Factor Release. Pharm Res 2010;**27**:468-479.
29 Bechet D, Couleaud P, Frochot C, Viriot ML, Guillemin F, Barberi-Heyob M. Nanoparticles as vehicles for delivery of photodynamic therapy agents. Trends Biotechnol 2008;**26**:612-621.

30 Couleaud P, Morosini V, Frochot C, Richeter S, Raehm L, Durand JO. Silica-based nanoparticles for photodynamic therapy applications. Nanoscale 2010;**2**:1083-1095.
31 Couleaud P, Bechet D, Vanderesse R, Barberi-Heyob M, Faure AC, Roux S, et al. Functionalized silica-based nanoparticles for photodynamic therapy. Nanomedicine (Lond)2011;**6**:995-1009.
32 Chin R, Ward R, Keyes JW, Choplin RH, Reed JC, Wallenhaupt S, et al. Mediastinal staging of non-small-cell lung cancer with positron emission tomography. Am J Respir Crit Care Med 1995;**152**:2090-2096.
33 Vansteenkiste JF, Stroobants SG, De Leyn PR, Dupont PJ, Bogaert J, Maes A, et al. Lymph node staging in non-small-cell lung cancer with FDG-PET scan: a prospective study on 690 lymph node stations from 68 patients. J Clin Oncol 1998;**16**: 2142-2149.
34 Weng E, Tran L, Rege S, Safa A, Sadeghi A, Juillard G, et al. Accuracy and clinical impact of mediastinal lymph node staging with FDG-PET imaging in potentially resectable lung cancer. Am J Clin Oncol 2000;**23**:47-52.
35 Schneider R, Schmitt F, Frochot C, Fort Y, Lourette N, Guillemin F, et al. Design, synthesis, and biological evaluation of folic acid targeted tetraphenylporphyrin as novel photosensitizers for selective photodynamic therapy. Bioorg Med Chem 2005;**13**:2799-2808.
36 Hennig J, Nauerth A, Friedburg H, Ratzel D. New rapid imaging procedure for nuclear spin tomography. Radiologe 1984;24:579-580.
37 Wong EC, Buxton RB, Frank LR. Implementation of quantitative perfusion imaging techniques for functional brain mapping using pulsed arterial spin labeling. NMR Biomed 1997;**10**:237-249.
38 Gruetter R. Automatic, localized in vivo adjustment of all first- and second-order shim coils. Magn Reson Med 1993;**29**:804-811.
39 Kopelman R, Koo, YEL, Philbert M, Moffat BA, Reddy GR, McConville P, et al. Multifunctional nanoparticle platforms for in vivo MRI enhancement and photodynamic therapy of a rat brain cancer. J Magn Magn Mat 2005;**293**:404-410.
40 Ross B, Rehemtulla A, Ko YEL, Reddy R, Kim G, Behrend C, et al. Photonic and magnetic nanoexplorers for biomedical use: from subcellular imaging to cancer diagnostics and therapy. Nanobiophotonics Biomed Appl 2004;**5331**:76-83.
41 Stuchinskaya T, Moreno M, Cook MJ, Edwards DR, Russell DA. Targeted photodynamic therapy of breast cancer cells using antibody-phthalocyanine-gold nanoparticle conjugates. Photochem Photobiol Sci 2011;**10**:822-831.
42 Porkka K, Laakkonen P, Hoffman JA, Bernasconi M, Ruoslahti E. A fragment of the HMGN2 protein homes to the nuclei of tumor cells and tumor endothelial cells in vivo. Proc Natl Acad Sci 2002;**99**:7444-7449.
43 Reddy GR, Bhojani MS, McConville P, Moody J, Moffat BA, Hall DE, et al. Vascular targeted nanoparticles for imaging and treatment of brain tumors. Clin. Cancer Res. 2006;**12**:6677-6686.
44 Hah HJ, Kim G, Lee Y-EK, Orringer DA, Sagher O, Philbert MA, et al. Methylene blue-conjugated hydrogel nanoparticles and tumor-cell targeted photodynamic therapy. Macromol Biosci 2011;**11**:90-99.
45 Qin M, Hah HJ, Kim G, Nie G, Lee Y-EK, Kopelman R. Methylene blue covalently loaded polyacrylamide nanoparticles for enhanced tumor-targeted photodynamic therapy. Photochem Photobiol Sci 2011;**10**:832-841.
46 Chen B, Pogue BW, Hoopes PJ, Hasan T. Vascular and cellular targeting for photodynamic therapy. Crit. Rev. Eukaryot. Gene Expr 2006;**16**:279-305.
47 Benachour H, Sève A, Bastogne T, Frochot C, Vanderesse R, Jasniewski J, et al. Multifunctional Peptide-conjugated hybrid silica nanoparticles for photodynamic therapy and MRI. Theranostics. 2012;**2**:889-904.
48 Maeda H. The enhanced permeability and retention (EPR) effect in tumor vasculature: The key role of tumor-selective macromolecular drug targeting. Adv Enzyme Regul 2001;**41**:189-207.
49 Maeda H, Wu J, Sawa T, Matsumura Y, Hori K. Tumor vascular permeability and the EPR effect in macromolecular therapeutics: a review. J Control Release 2000;**65**:271-284.
50 Lux F, Mignot A, Mowat P, Louis C, Dufort S, Bernhard C, et al. Ultrasmall rigid particles as multimodal probes for medical applications. Angew Chem Int Ed Engl 2011;**50**:12299-12303.

51 Le Duc G, Miladi I, Alric C, Mowat P, Bräuer-Krisch E, Bouchet A, et al. Toward an image-guided microbeam radiation therapy using gadolinium-based nanoparticles. ACS Nano 2011;**5**:9566-9574.
52 Lehtimäki KK, Valonen PK, Griffin JL, Väisänen TH, Gröhn OHJ, Kettunen MI, et al. Metabolite changes in BT4C rat gliomas undergoing ganciclovir-thymidine kinase gene therapy-induced programmed cell death as studied by 1H NMR spectroscopy in vivo, ex vivo, and in vitro. J Biol Chem 2003;**278**:45915-45923.
53 Hakumäki JM, Poptani H, Sandmair A-M, Ylä-Herttuala S, Kauppinen RA. 1H MRS detects polyunsaturated fatty acid accumulation during gene therapy of glioma : Implications for the in vivo detection of apoptosis. Nat Med 1999;**5**:1323-1327.
54 Valonen PK, Griffin JL, Lehtimäki KK, Liimatainen T, Nicholson JK, Gröhn OHJ, et al. High-resolution magic-angle-spinning 1H NMR spectroscopy reveals different responses in choline-containing metabolites upon gene therapy-induced programmed cell death in rat brain glioma. NMR Biomed. 2005;**18**:252-259.
55 Van Au Duong M, Audoin B, Le Fur Y, Confort-Gouny S, Malikova I, Soulier E, et al. Relationships between gray matter metabolic abnormalities and white matter inflammation in patients at the very early stage of MS : a MRSI study. J Neurol 2007;**254**:914-923.
56 Evans S, Matthews W, Perry R, Fraker D, Norton J, Pass HI. Effect of photodynamic therapy on tumor necrosis factor production by murine macrophages. J Natl Cancer Inst 1990;**82**:34-39.
57 Seshadri M, Bellnier D. 5, 6-Dimethylxanthenone-4-Acetic Acid Improves the Antitumor Efficacy and Shortens Treatment Time Associated with Photochlor-sensitized Photodynamic Therapy. Photochem. Photobiol. 2009;**85**:50-56.
58 Szotowski B, Antoniak S, Poller W, Schultheiss HP, Rauch U. Procoagulant soluble tissue factor is released from endothelial cells in response to inflammatory cytokines. Circ Res 2005;**96**:1233-1239.
59 Angell-Petersen E, Spetalen S, Madsen SJ, Sun CH, Peng Q, Carper SW, et al. Influence of light fluence rate on the effects of photodynamic therapy in an orthotopic rat glioma model. J Neurosurg 2006;**104**:109-117.
60 Angell-Petersen E, Hirschberg H, Madsen SJ. Determination of fluence rate and temperature distributions in the rat brain; implications for photodynamic therapy. J Biomed Opt 2007;**12**:14003.
61 Frahm J, Haase A, Matthaei D. Rapid NMR imaging of dynamic processes using the FLASH technique. Magn Reson Med 1986;**3**:321-327.
62 Mansfield P, Maudsley A. Planar spin imaging by NMR. J Magn Reson 1977;**27**:101-119.
63 Kim SG, Tsekos N V. Perfusion imaging by a flow-sensitive alternating inversion recovery (FAIR) technique: application to functional brain imaging. Magn Reson Med 1997;**37**:425-435.
64 Bottomley PA. Spatial Localization in NMR Spectroscopy in Vivo. Ann N Y Acad Sci 1987;**508**:333-348.